SNAME Maritime Convention 2020 – A Virtual Event
29 September- 2 October

www.sname.org

2D CFD Studies on Effects of Leading-Edge Propeller Manufacturing Defects on Cavitation Performance

Shanqin Jin[1] (V)**, Ruosi Zha**[1] (V)**, Heather Peng**[1] (M)**, Wei Qiu**[1] (FL), and **Slobodan Gospodnetic**[2] (M)
1. Department of Ocean and Naval Architectural Engineering, Memorial University of Newfoundland, St. John's, NL, Canada.
2. Dominis Engineering, Ottawa, ON, Canada.

In this work, effects of manufacturing defects on the cavitation performance of a propeller blade section were studied with 2-D steady RANS solvers. DTMB modified NACA66 a = 0.8 sections without and with leading edge (LE) defects were investigated at various angles of attack using Star-CCM+ on structured grids. Using the best-practice settings, verification studies were carried out for the cavitation buckets of a 20% thick 2% camber section without a defect. The main body of this work examines minimum pressure coefficients on a 4.16% thick 1.4% camber section with and without defects near the LE. These lead to conclusions about the relative cavitation inception speeds of defective sections and the consequences for manufacturing tolerances.

KEY WORDS: CFD, propeller manufacturing defect, cavitation.

NOMENCLATURE

α	angle of attack
ϵ	turbulence dissipation rate
μ	dynamic viscosity of water
ρ	density of water
υ	kinematic viscosity of water
ω	specific turbulence dissipation rate
AR	aspect ratio of a structured grid
c	chord length
C_d	drag coefficient
C_l	lift coefficient
C_p	pressure coefficient = $(p - p_\infty)/(0.5\rho U^2)$
$C_{p_{min}}$	minimum pressure coefficient
f	maximum camber of a foil section
ISR	Inception speed ratio
k	turbulence kinetic energy
LE	leading edge
p	pressure
p_a	air pressure
p_∞	pressure of far field
p_v	vapor pressure of water
R	radius of circular domain
Re	Reynolds number = Uc/ν
RANS	Reynolds averaged Navier-Stokes equations
SR	stretching ratio
t	maximum thickness of a foil section
TE	trailing edge
U	flow velocity
y^+	dimensional first-grid spacing

INTRODUCTION

Underwater radiated noise (URN) from ships is being recognized as a world-wide problem since underwater noise from shipping is increasingly being considered as a significant and omnipresent pollutant with the potential to impact marine ecosystems on a global scale. Continued growth in the number of ships will significantly increase the total volume of noise generated by the global shipping fleet. Projections suggest that URN level could increase by as much as a factor of 1.9 of the current level by the year 2030 (Southall et al., 2017). The URN of a ship is caused mainly by the propeller and the main machinery. The European Union's collaborative research project AQUO (Achieve Quieter Oceans) has provided valuable insight into the relative contribution of each source of noise generated by different types of ships (AQUO, 2015). A significant conclusion of the study is that propeller cavitation is the most important source of noise for ferries and cruise vessels at normal operating speeds. The noise levels from a ship jump substantially when propeller cavitation begins.

Many studies have been carried out to investigate effects of design parameters on cavitation and efficiency performance of a propeller with an objective to avoid or control vortex cavitation and to improve its efficiency. However, little effort has been made to understand the impact of propeller manufacturing tolerances or defects on the propeller performance, and no paper in the public literature was found to address this issue. A preliminary computational fluid dynamics (CFD) study carried out by Hally (2018) indicates that the manufacturing defects potentially have large impact on propeller cavitation performance. In a recent workshop, it was suggested to study the

effect of manufacturing defects on propeller cavitation performance (CISMaRT, 2018) with an objective to reduce URN.

Manufacturing tolerances for new ship propellers are specified by organizations, such as International Standards Organization (ISO), which defines the manufacturing standards for propeller construction, and the Naval Sea Systems Command, USA (NAVSEA), which provides manufacturing standards for US Navy's ship construction (2004). The ISO 484-1 and ISO 484-2 standards for manufacturing tolerances for ship propellers (2015) were established in 1981 by adopting an ISO Recommendation of 1966. ISO 484-1 is applicable to propellers with diameters greater than 2.5 m, while ISO 484-2 is applicable to propellers with diameters from 0.8 m to 2.5 m. There are four classes of tolerances in each standard. Each tolerance class is intended for a certain type of vessels. Among the four classes, Class S denotes the smallest tolerance and hence the highest precision.

The majority of propellers manufactured today are hand- or robotic finished from castings which are rough machined using Computer Numerical Control (CNC) (van Beek and Janssen, 2000; Janssen and Leever, 2017). Blade edges and tips, the most sensitive parts of the geometry of a propeller, are made to conform to templates of their required form using manual grinding. Manual grinding of propeller surfaces introduces inaccuracies and deviations from design, which could lead to degradation of propeller performance in terms of efficiency, cavitation and noise.

Manufacturers could take various measures to finish machining propellers. Dominis Engineering, for example, uses a CNC milling process which eliminates manual grinding of blade edges and tips (Gospodnetic and Gospodnetic, 1996; Gospodnetic, 2013). This process has put possible manufacturing tolerances in a new, more accurate era (Gospodnetic, 2015; Tremblay and Gospodnetic, 2017), which better complements today's sophisticated propeller design tools. In light of these changes, it is necessary to better understand the sensitivity of propeller performance to manufacturing defects so that manufacturers can develop appropriate, cost-effective processes; naval architects can better specify tolerances to their needs; and owners and regulators can rest assured that vessels will meet their requirements.

The objective of the present work is to study the cavitation performance of an ideal propeller blade section (as designed) and "as-built" propeller blade sections with various sizes of defects. This paper is focused on examining effects of leading-edge (LE) manufacturing defects on the cavitation performance with CFD methods. Cavitation and efficiency performance of 2-D modified NACA66 foil sections with and without LE defects are compared at various angles of attack. All the chosen sizes of defects in the present studies are within the limits of ISO 484-1 Class S tolerances. CFD simulations were carried out using the steady RANS solver in Star-CCM+ on structured grids.

Convergence studies were first performed for four foils without and with defects using rectangular and circular computational domains. Effects of simulation parameters, such as domain size, grid resolution, grid distribution, grid stretching ratio, grid aspect ratio, first-grid spacing, y^+, and turbulence model, on the solutions were carefully examined. The total number of simulation cases is over 1,000. Based on the results of convergence studies, the best-practice settings for 2-D simulations with the steady RANS solver in Star-CCM+ were proposed.

Using the best-practice settings, verification studies were carried out for the cavitation buckets of a DTMB modified NACA66 section $a = 0.8$ ($t/c = 0.2$, $f/c = 0.02$) without defect by comparing the RANS results with the potential-flow solutions (Brockett,1966) and the RANS results with ANSYS CFX (Hally, 2018). Note that t, f and c denote the maximum thickness, the maximum camber and the chord length of a foil section, respectively. Furthermore, the minimum pressure coefficients for the DTMB modified NACA66 sections $a = 0.8$ ($t/c = 0.0416$, $f/c = 0.014$) with three different sizes of defects near LE, representing three levels of manufacturing tolerances within Class S, were compared at various angles of attack. As all sections herein are DTMB modified NACA66 a=0.8 sections, they will be referred to only by their (t/c, f/c) and by the size of their defect (if any) in the following sections.

THEORETICAL METHODOLOGY

Governing equations for the RANS solver and turbulence modeling in Star-CCM+ are summarized below.

Governing Equations

The RANS equations for the incompressible viscous flow are:

$$\frac{\partial u_i}{\partial x_i} = 0 \tag{1}$$

$$\rho \frac{\partial u_i}{\partial t} + \rho u_j \frac{\partial u_i}{\partial x_j} = -\frac{\partial p}{\partial x_i} + \frac{\partial}{\partial x_j}\left[\mu\left(\frac{\partial u_i}{\partial x_j} + \frac{\partial u_j}{\partial x_i}\right)\right] + \frac{\partial}{\partial x_j}\left(-\rho\overline{u_i' u_j'}\right) \tag{2}$$

where $u_{i,\ i=1,2}$, denotes the velocity components along x- and y-axis, respectively, for a two-dimensional flow, and $-\rho\overline{u_i' u_j'}$ are the Reynolds stresses. The Reynolds stresses can be solved using the eddy viscosity turbulence models or Reynolds stress models.

Turbulence Modeling

Four eddy viscosity turbulence models were considered in this work: Spalart-Allmaras (SA), k-ϵ, k-ω, and the Shear Stress Transport (SST) k-ω. In the eddy viscosity models, it is assumed that the Reynolds stresses are related to the mean velocity gradients, the turbulence kinetic energy, and the eddy viscosity, i.e.,

$$-\rho\overline{u_i' u_j'} = \mu_t\left(\frac{\partial u_i}{\partial x_j} + \frac{\partial u_j}{\partial x_i}\right) - \frac{2}{3}\rho k \delta_{ij} \tag{3}$$

where μ_t is the eddy viscosity, δ_{ij} is the Kronecker delta, $k = 1/2\,\overline{u_i' u_j'}$ is the turbulent kinetic energy that can be solved from the transport equations. The Reynolds stress tensor is linearly proportional to the mean strain rate.

The one-equation model SA (Spalart, 1992) used by Star-CCM+ solves a transport equation for the modified diffusivity, $\tilde{\nu}$, to determine the turbulence eddy viscosity, μ_t, i.e.,

$$\mu_t = \rho f_{\nu 1} \tilde{\nu} \tag{4}$$

where $f_{\nu 1}$ is a damping function and the transport equation for the modified diffusivity is:

$$\frac{\partial}{\partial t}(\rho\tilde{\nu}) + \nabla \cdot (\rho\tilde{\nu}\bar{\mathrm{v}}) = \frac{1}{\sigma_{\tilde{\nu}}}\nabla \cdot [(\mu + \rho\tilde{\nu})\nabla\tilde{\nu}] + P_{\tilde{\nu}} + S_{\tilde{\nu}} \tag{5}$$

where $\bar{\mathrm{v}}$ is the mean velocity, $\sigma_{\tilde{\nu}}$ is a model coefficient, $P_{\tilde{\nu}}$ is the production term, and $S_{\tilde{\nu}}$ is the source term. While the SA model has good convergence and robustness for specific flows: flows with mild separation (such as flow past a wing), wake, mixing layer and radial jet flows, the turbulence length and time scales are not well defined. As in two-equation models, in which both the velocity and length scales are solved using separate transport equations. The turbulence length scale is estimated from the kinetic energy and its dissipation rate.

For the standard k-ϵ model (Jones and Launder, 1972), the turbulent eddy viscosity is calculated as:

$$\mu_t = \rho C_\mu f_\mu k T \tag{6}$$

where C_μ is a model coefficient, f_μ is a damping function, and T is the turbulent time scale calculated by:

$$T = \max\left(T_e, C_t\sqrt{\frac{\nu}{\epsilon}}\right) \tag{7}$$

where T_e is the large-eddy time scale and C_t is a model coefficient. The turbulent kinetic energy, k, and the turbulence dissipation rate, ϵ, are solved from transport equations.

In the standard k-ω model (Wilcox, 1988), the turbulent eddy viscosity is related to the turbulence kinetic energy, k, and the specific turbulence dissipation rate, ω, which is also referred to the mean frequency of the turbulence. The turbulent eddy viscosity is calculated as:

$$\mu_t = \rho k T \tag{8}$$

where $T = \alpha^*/\omega$ is the turbulence time scale in the standard k-ω model and α^* is a model coefficient. The turbulent kinetic energy, k, and the specific dissipation rate, ω, are solved from two transport equations. The k-ω model predicts strong vortices and the near-wall interactions more accurately than the k-ϵ model. The original k-ω model over-predicts shear stresses of adverse pressure gradient boundary layers, and it is sensitive to initial conditions and inlet boundary conditions.

For the SST k-ω model, the transport equations are the same as those of the standard k-ω model when the damped cross-diffusion derivative term is set to zero in the near field. In the far field, the transport equations are the same as those of the standard k-ϵ model, which can avoid the problem that the model is too sensitive to the inlet turbulence properties. Detailed formulations can be found in the work by Menter (1993). By introducing the transport of the turbulence shear stress, the SST k-ω model improves the prediction of the onset and the flow separation under adverse pressure gradients.

In the Reynolds stress models (RSM), the transport equations are solved for all the components of the Reynolds stress tensor and the turbulence dissipation rate, i.e.,

$$\frac{\partial}{\partial t}\left(\rho\overline{u_i'u_j'}\right) + \frac{\partial}{\partial x_k}\left(\rho u_k \overline{u_i'u_j'}\right) = P_{ij} + F_{ij} + D_{ij}^T + \phi_{ij} - \epsilon_{ij} \tag{9}$$

where P_{ij} is the stress production, F_{ij} is the rotation production, D_{ij}^T is the turbulent diffusion, ϕ_{ij} is the pressure strain tensor, and ϵ_{ij} is the dissipation rate tensor. Two Reynolds stress models are used in the present work: the elliptic bending model, EB-RSM, and the linear pressure-strain two-layer model, LPS-RSM.

NUMERICAL SIMULATIONS

Extensive numerical simulations were carried out using the steady RANS solver in Star-CCM+ on structured grids for (t/c = 0.0416, f/c = 0.014) without and with LE defects in an infinite domain.

In addition, simulations were carried out for (t/c = 0.2, f/c = 0.02) without defect with an objective to verify the numerical results by comparing them with the potential-flow solutions and the RANS results with ANSYS CFX.

In the present work, the chosen modified NACA66 foils have a chord length of 1,000 mm. The Reynolds number is 3.0×10^7.

Coordinate System

The coordinate system for 2-D simulations is presented in Fig. 1. The origin, O, is at the leading edge of the foil. The OX axis is from the leading edge to the trailing edge (TE) along the chord line and the OY axis is perpendicular to the chord line.

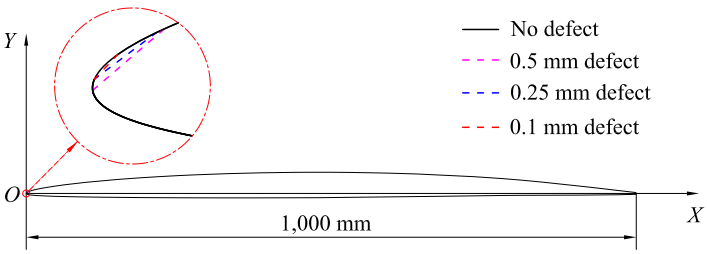

Figure 1: Foils (t/c = 0.0416, f/c = 0.014) without and with LE defects

Leading Edge Manufacturing Defects

All the defects considered in present work are within ISO Class S. A leading edge defect is determined by measuring the difference between the template and the manufactured blade section. According to ISO 484 (2015), Class S tolerances for LE deviations are defined as ±0.5 mm for a 1-part template or ±0.25 mm for the 3-part template (see Fig. 2).

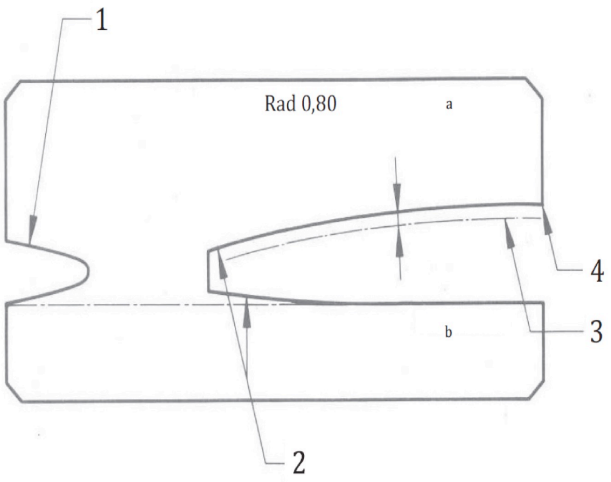

Figure 2: 3-part templates (ISO, 2015)

Figure 3 shows how a foil with 0.25 mm LE defect is measured using a 3-part template (note that the short nose template was omitted here for clarity).

Details of LE geometry for the foil (t/c = 0.0416, f/c = 0.014) with and without defects are shown in Fig. 4. Dimensions of LE defects are given in Table 1. Note that all the defects are within Class S.

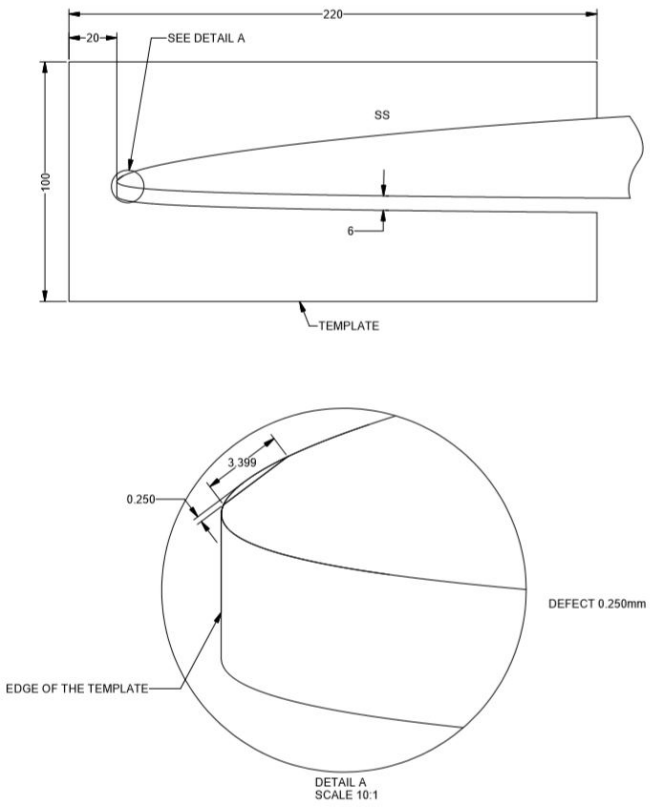

Figure 3: Template and the foil section with 0.25 mm deviation

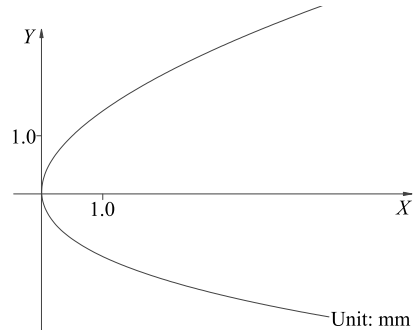

(a) No defect

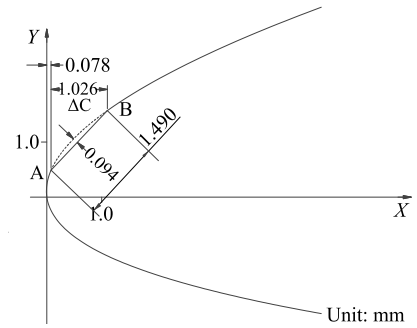

(b) 0.1mm defect

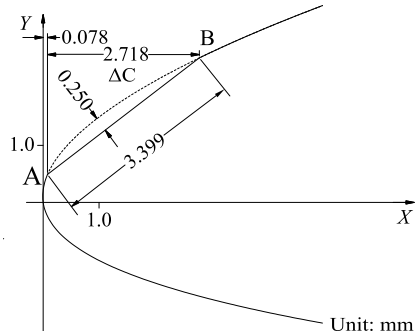

(c) 0.25 mm defect

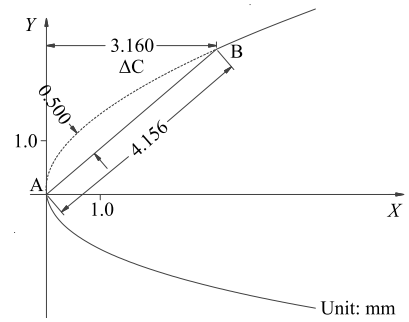

(d) 0.5mm defect

Figure 4: LE geometry of the foil (t/c = 0.0416, f/c = 0.014) with and without defects

Table 1. Dimensions of LE defects of foils (Unit: mm)

Defect	Point A		Point B		Length	ΔC
	X	Y	X	Y		
0.094	0.078	0.490	1.104	1.571	1.490	1.026
0.250	0.078	0.490	2.796	2.531	3.399	2.718
0.500	0.000	0.000	3.160	2.700	4.156	3.160

Computational Domain

The computational domain must be sufficiently large to represent the infinite fluid domain. It is preferable to use structured grids for simulations to achieve greater accuracy. The geometry of the domain should be chosen in such a way that generated structured grids are of high quality. To generate the grids for foils with defects, adequate grids must be distributed on the foil surface, especially near LE defects, to resolve the flow details. On the other hand, since a large computational domain is required, the grid spacing needs to be increased when approaching to the domain boundaries for the purpose of computing efficiency. These lead to some challenges in generating structured grids.

Both rectangular and circular computational domains were investigated. Extensive studies have shown that the circular domain provided grids of greater quality than rectangular domains and hence greater accuracy in solutions. Therefore, the circular domain with the O-type topology as shown in Fig. 5 was employed. Six domain sizes with radii (R) of 6, 12, 18, 24, 30 and 36 chord length were investigated in the present work.

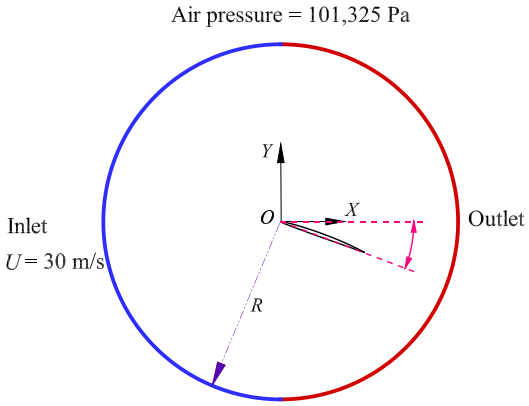

Figure 5: Circular computational domain

Boundary conditions are also presented in Fig. 5. Note that the hydrostatic pressure was not taken into account in the present simulations. The pressure boundary condition with $p = p_a$ was specified on the outlet. A no-slip wall boundary condition was imposed on the surface of the foil section. The Reynolds number for all cases was Re = 3.0×10^7. At the inlet boundary, a uniform velocity of $U = 30$ m/s was specified.

Grid Generation

The generation of structured grids is dependent on the specified y^+, the grid aspect ratio, and the grid stretching ratio. The non-dimensional first-grid spacing, y^+, is estimated by:

$$y^+ = \sqrt{\frac{0.013U^2}{Re^{1/7}}}\frac{\Delta S}{\nu} \tag{10}$$

where ΔS is the height of the first grid near the wall. Note that ΔS is measured from the center of the grid cell in Star-CCM+.

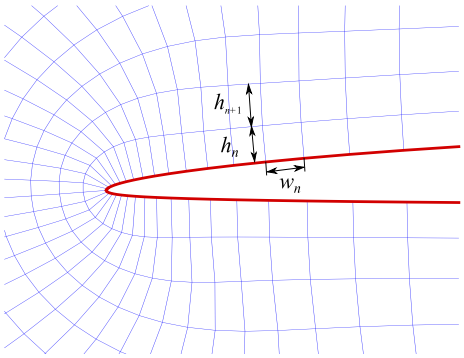

Figure 6: Definition of grid geometry

The grid aspect ratio (AR) is defined as the maximum ratio of grid width to height. As shown in Fig. 6, the AR of the n^{th} grid is determined as:

$$AR = w_n/h_n \tag{11}$$

where w_n and h_n are the grid width and height, respectively.

The grid stretching ratio (SR) is defined as the ratio of heights of adjacent cells. As shown in Fig. 6, SR of the n^{th} grid is given as:

$$SR = h_{n+1}/h_n \tag{12}$$

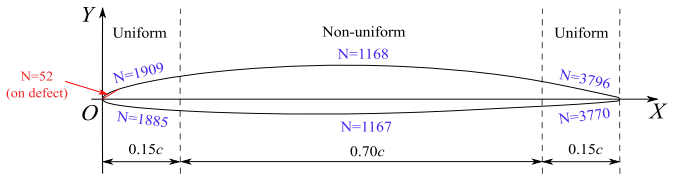

Figure 7: Grid distribution on the surface of the foil with 0.5 mm defect

As shown in Fig. 7, both face and back of the foil are divided into three segments. Uniform grids are distributed on the leading and the TE segments while non-uniform grids are on the middle segment.

As an example, grids near the leading edge and the tailing edge for the foil with 0.5 mm LE defect are shown in Fig. 8. For this case, the first grid spacing, y^+, is 1.0. The total number of grids on the foil surface is 13,695. The corresponding numbers of grids on the back/the face of the LE segment, on the TE segment, and on the middle segment are shown in Fig. 7. The corresponding grid aspect ratios on the leading edge, the trailing edge and the middle segments are 40, 20 and 300, respectively. Note that 52 grids were distributed over the 0.5 mm defect to resolve the flow details. Uniform grids with AR = 20 were distributed near the trailing edge to improve the simulation of vortex flow.

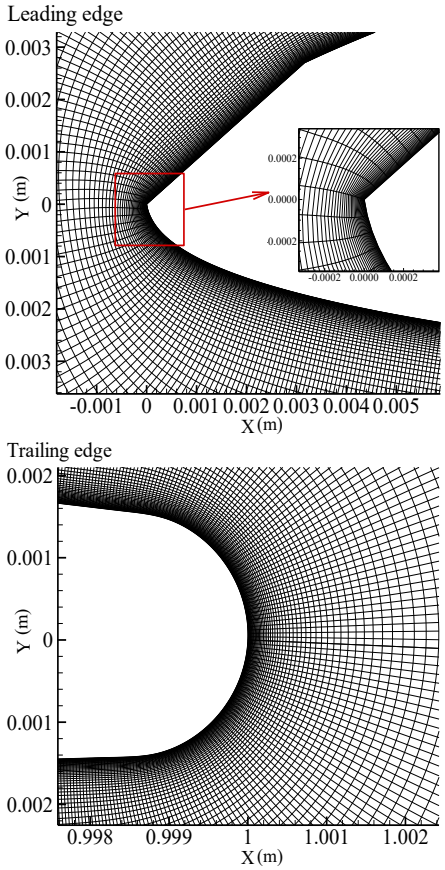

Figure 8: Grids near the leading edge and the trailing edge

Convergence Criteria

Two levels of convergence criteria were applied in the present studies, including:

- Residuals, defined as normalized root-mean-squared values in Star-CCM+, are used as the first convergence criterion. Three orders of magnitude reduction in residuals are considered as an acceptable level. Note that residuals are not the only measure for convergence. The initial values strongly influence the residuals. If the initial solution satisfies the discretized equations very well, the residuals would not reduce significantly. Therefore, it is necessary to examine the convergence of lift, drag and pressure coefficients.
- For the convergence of lift, drag and pressure coefficients, the changes between their values at the present and previous iterations are used as indicators after the residual criteria are satisfied. For the lift and drag coefficients, it is considered acceptable if the changes between two iterations are in the order of 10^{-6}. For the minimum pressure coefficient, the acceptable value is in the order of 10^{-5}.

The maximum number of iterations was set as 40,000 for all simulations. Residuals and changes in lift, drag and minimum pressure coefficients were then checked against the convergence criteria described above.

Simulation Parameters and Cases

The air pressure is set as p_a = 101,325 Pa. The density of water is ρ = 1,000 kg/m^3 and the kinematic viscosity of water is 1.0×10^{-6} m^2/s. Over 1,000 cases at various angles of attack were simulated using different turbulence models, first-grid spacings, grid aspect ratios, grid stretching ratios, and numbers of grids near the LE and the defect.

A summary of simulation cases using the circular computational domain is provided below:

- Domain sizes in terms of radius of domain: 6 m, 12 m, 18 m, 24 m, 30 m and 36 m.
- Grid stretching ratios: 1.1 and 1.2.
- Grid aspect ratios at LE: 320.0, 160.0, 113.12, 80.0, 56.56 and 40.0.
- Grid aspect ratios at TE: 120.0, 80.0, 60.0, 40.0, 30.0 and 20.0.
- First-grid spacing, y^+: 0.5, 0.707, 1.0, 1.414, 2.0, 2.828, 4.0, 5.0, 10.0, 15.0, 30.0, 60.0, 90.0 and 120.0.
- Turbulence models: Spalart-Allmaras one-equation model, k-ϵ, $k-\omega$ and SST $k-\omega$ two-equation models; and elliptic blending and linear pressure-strain Reynolds stress models.

In these convergence studies, the number of grids ranges from 791,415 to 2,013,312.

Summary of Best-Practice Settings

The numbers of grids for the foil without/with defect are summarized in Table 2. Based on extensive convergence studies, best-practice settings for 2-D simulations with the Star-CCM+ steady RANS solver are determined and presented in Table 3. Other default settings for the solver are summarized in Table 4.

Table 2. Number of grids for (t/c = 0.0416, f/c = 0.014) with and without defects

	No defect	0.5 mm defect	0.25 mm defect	0.1 mm defect
Number of grids over defect	-	52	42	19
Number of grids on the back	3,044	3,041	3,043	3,043
Number of grids on the face	3,014	3,014	3,014	3,014
Number of grids on foil surface	6,058	6,055	6,057	6,057
Total number of grids	890,526	890,085	890,379	890,379

Table 3. Best-practice settings for (t/c = 0.0416, f/c = 0.014) with and without defects

	Best-practice Settings
Domain type	Circular
Domain size	R = 24 m
Grid topology	O-type
y^+	1.0
Grid stretching ratio	1.1
Grid aspect ratio near LE	40
Grid aspect ratio near TE	120
Minimum number of grids over 0.5 mm defect	52
Minimum number of grids over 0.25 mm defect	43
Minimum number of grids over 0.1 mm defect	19
Wall treatment	low y^+ wall treatment
Turbulence model	Standard $k-\omega$

Table 4. Default settings used in the present simulations with Star-CCM+

Simulation Parameters	Default Settings
Convection scheme	2^{nd}-order upwind
Gradient method	Hybrid Gauss-Least squares method
Limiter method	Venkatakrishnan method
Custom accuracy level selector	2^{nd}-order
Reference pressure	101,325 Pa
Initial turbulence intensity, I	1%
Initial turbulent viscosity ratio, μ_t/μ	10.0
Linear solver	Algebraic multigrid methods (AMG)
Relaxation scheme	Gauss-Seidel
Under-relaxation factor for velocity	0.4
Under-relaxation factor for pressure	0.1
Under-relaxation factor for turbulence	0.8
Convergence tolerance	0.1

SIMULATION RESULTS

With the best-practice settings summarized in the previous section, numerical simulations were carried out for (t/c = 0.2, f/c = 0.02) without defect and (t/c = 0.0416, f/c = 0.014) without and with LE defects in an infinite domain. The simulation results of cavitation buckets, pressure, residuals, C_d and C_l are presented in this section and the effect of LE defect on cavitation inception speed and efficiency are discussed.

Cavitation Buckets for (t/c = 0.2, f/c = 0.02) without Defect

The predicted cavitation buckets of (t/c = 0.2, f/c = 0.02) without defect in terms of the negative minimum pressure coefficient at angles of attack from -5° to 6° are presented in Fig. 9 and compared with the potential-flow solutions (Brockett, 1966) and the numerical results with ANSYS CFX and TRANSOM by DRDC (Hally, 2018). The agreement is in general good.

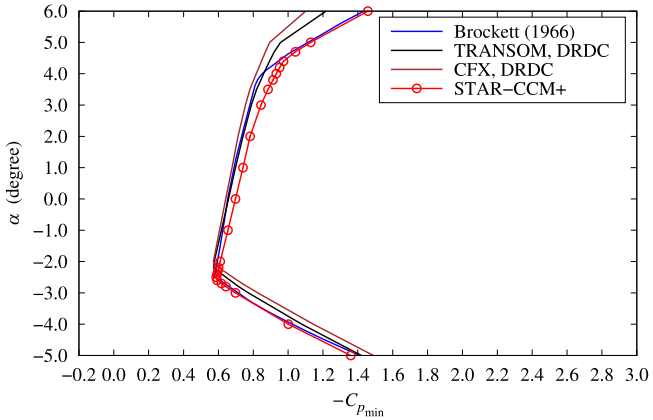

Figure 9: Cavitation buckets for (t/c = 0.2, f/c = 0.02) without defect

Cavitation Buckets for (t/c = 0.0416, f/c = 0.014) without and with LE Defect

Cavitation buckets were compared for (t/c = 0.0416, f/c = 0.014) without defect and with three different LE defects (0.5 mm, 0.25 mm and 0.1 mm) at a number of angles of attack. As shown in Fig. 10, the cavitation buckets are narrowed by the defects at the LE in the region of typical propeller design. In other words, the incipient cavitation speed is reduced by the LE defect. Note that dashed lines denote one example in the typical design range.

Table 5. Angles of attack for (t/c = 0.0416, f/c = 0.014) with and without defects

Angle of attack, α (degree)	-4.00, -3.00, -2.75, -2.50, -2.25, -2.00, -1.75, -1.50, -1.25, -1.00, -0.75, -0.50, -0.40, -0.30, -0.20, -0.10, 0.00, 0.10, 0.20, 0.25, 0.30, 0.40, 0.50, 0.60, 0.70, 0.80, 0.90, 1.00, 1.25, 1.50, 1.75, 2.00, 2.25, 2.50, 2.75, 3.00, 4.00

Minimum pressure coefficients and their locations on the foil surface, residuals of simulations, and the convergence of drag and lift coefficients are provided in the following subsections.

Pressure Contours and Streamlines

As one example in the typical propeller design range, the contours of pressure coefficient and streamlines near the LE at $\alpha = 0.8^\circ$ for (t/c = 0.0416, f/c = 0.014) with no defect, 0.5 mm defect, 0.25 mm defect and 0.1 mm defect are presented in Fig. 11.

It can be observed that the defect led to lower pressure near the LE. Although locations of the minimum pressure depend on the size of a defect, they are all located close to the upper end of the flat defect. For example, the upper end point of the 0.5 mm defect is (0.00316 m, 0.0027 m) and the location of the minimum pressure is at (0.00323 m, 0.00267 m) .

To further quantify the reduction of cavitation inception speed due to a defect, the cavitation inception speeds for the foils without defect and with defect can be denoted as U_0 and U', respectively, as follows:

$$U_0 = \sqrt{\frac{2(p_v - p_\infty)}{\rho C_{p_{min}}}} \tag{13}$$

$$U' = \sqrt{\frac{2(p_v - p_\infty)}{\rho C'_{p_{min}}}} \tag{14}$$

where p_v is 1705.8 Pa (vapor pressure of water at 15°C), $C_{p_{min}}$ and $C'_{p_{min}}$ are the minimum pressure coefficients for the foils without and with defect, respectively.

The cavitation inception speed ratio, *ISR*, is defined as

$$ISR = \frac{U'}{U_0} = \sqrt{\frac{C_{p_{min}}}{C'_{p_{min}}}} \tag{15}$$

Table 6 presents negative minimum pressure coefficients and their locations for the foils with no defect, 0.5 mm defect, 0.25 mm defect and 0.1 mm defect at $\alpha = 0.8^\circ$. The cavitation inception speed ratios and their reduction percentages with respect to the foil without defect (as designed) are also included in the table. It can be observed that even the smallest defect leads to a significant reduction in the cavitation inception speed (over 25% reduction for 0.1 mm defect) at angle of attack of 0.8°.

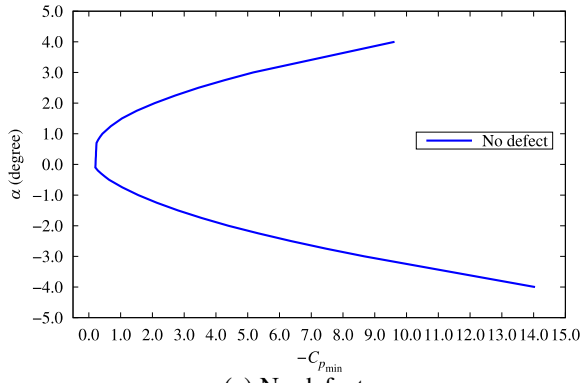

(a) No defect

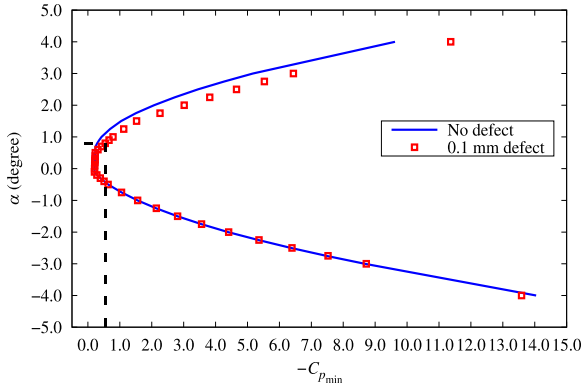

(b) 0.1 mm defect

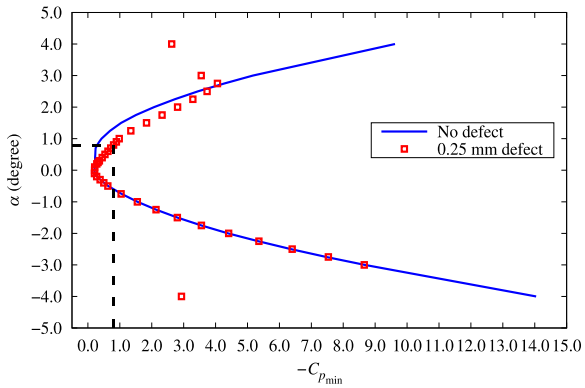

(c) 0.25 mm defect

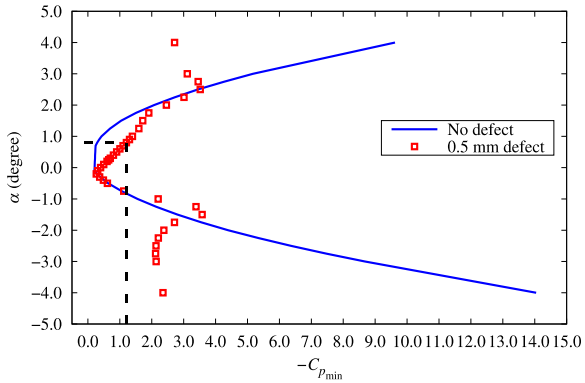

(d) 0.5 mm defect

Figure 10: Cavitation buckets for (t/c = 0.0416, f/c = 0.014) without and with LE defects

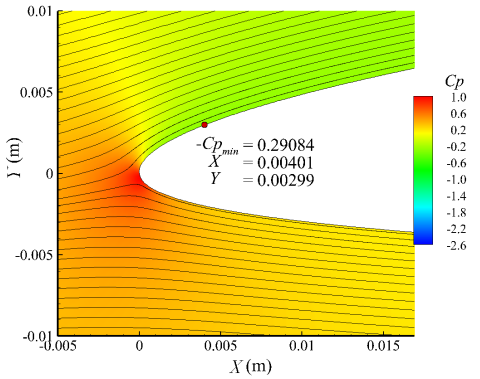

(a) No defect

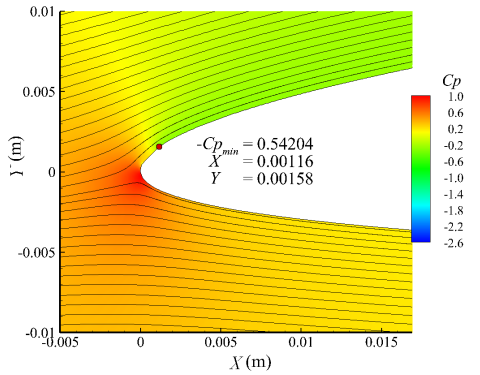

(b) 0.1 mm defect

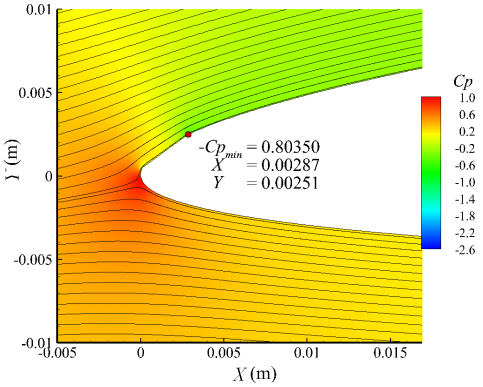

(c) 0.25 mm defect

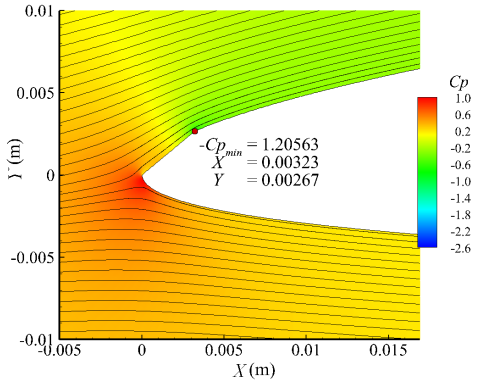

(d) 0.5 mm defect

Figure 11: Pressure coefficient contours and streamlines for (t/c = 0.0416, f/c = 0.014) at α = 0.8°

Table 6. Cavitation inception speed variations with defects for (t/c = 0.0416, f/c =0.014) at $\alpha = 0.8^{\circ}$

Foil	No defect	0.5 mm defect	0.25 mm defect	0.1 mm defect
$C_{p_{min}}$	-0.29084	-1.20563	-0.8035	-0.54204
Location (X, Y) (m)	(0.00401, 0.00299)	(0.00323, 0.00267)	(0.00287, 0.00251)	(0.00116, 0.00158)
Inception Speed (m/s)	26.173	12.855	15.753	19.179
ISR	1	0.491	0.602	0.733
Inception Speed Reduction Percentage	-	50.9%	39.8%	26.7%

Pressure Plots

Continuing with the above example, the pressure distributions near the LE at $\alpha = 0.8^{\circ}$ for the four foils, i.e., with no defect, 0.5 mm defect, 0.25 mm defect and 0.1 mm defect, are shown in Fig. 12. It was found that the pressures on the back were significantly changed by the defect near LE.

Results of Residuals, - $C_{p_{min}}$, C_d and C_l

In STAR-CCM+, the normalized Root Mean Squared value of residual for all cells is used to monitor the behavior of the solvers at each iteration. Residuals of simulations for the four foils with no defect, 0.5 mm defect, 0.25 mm defect and 0.1 mm defect at $\alpha = 0.8^{\circ}$ are shown in Fig. 13 as one example. Three orders of magnitude reduction in residuals were achieved. In these figures, the legend of "Continuity" denotes the residual for the continuity equation, "X-momentum" is the residual for the momentum equation (X-component), "Y-momentum" is the residual for the momentum equation (Y-component), "Tke" represents the residual for the transport equation of turbulence kinetic energy (k), and "Sdr" denotes the residual for the transport equation of specific dissipation rate (ω).

Table 7. Numerical results for (t/c = 0.0416, f/c = 0.014) at $\alpha = 0.8^{\circ}$

Foil	No defect	0.5 mm defect	0.25 mm defect	0.1 mm defect
$-C_{p_{min}}$	0.290840	1.205630	0.803500	0.542040
C_d	0.005468	0.005475	0.005474	0.005468
C_l	0.254443	0.254402	0.254437	0.254473
Change in $-C_{p_{min}}$ between two iterations	6×10^{-7}	6×10^{-7}	6×10^{-7}	6×10^{-7}
Change in C_d between two iterations	5×10^{-9}	0	0	0
Change in C_l between two iterations	2×10^{-7}	0	0	0

The corresponding iteration histories for the drag and lift coefficients are shown in Fig. 14, respectively. The negative minimum pressure coefficient, $-C_{p_{min}}$, the drag and lift coefficients, C_d, C_l, and their changes between the last two iterations are summarized in Table 7.

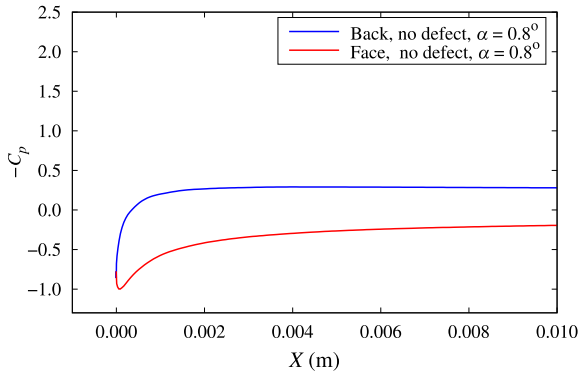

(a) No defect

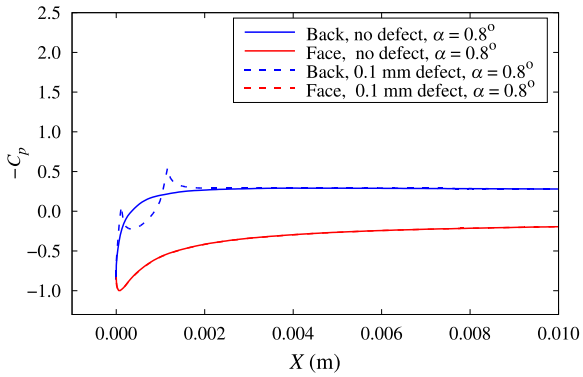

(b) 0.1 mm defect

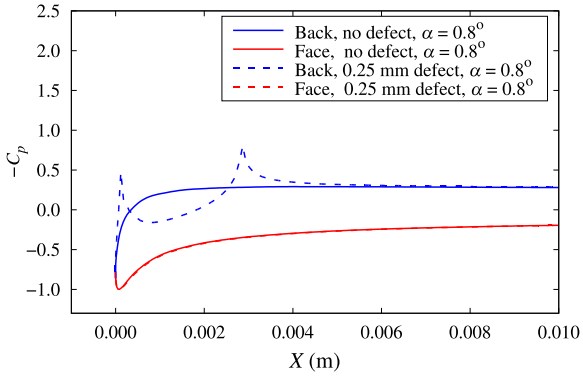

(c) 0.25 mm defect

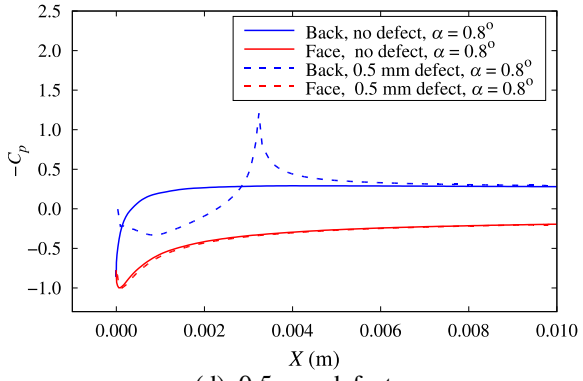

(d) 0.5 mm defect

Figure 12: Pressure distributions on the face and back of (t/c = 0.0416, f/c = 0.014) with and without defect at $\alpha = 0.8^{\circ}$

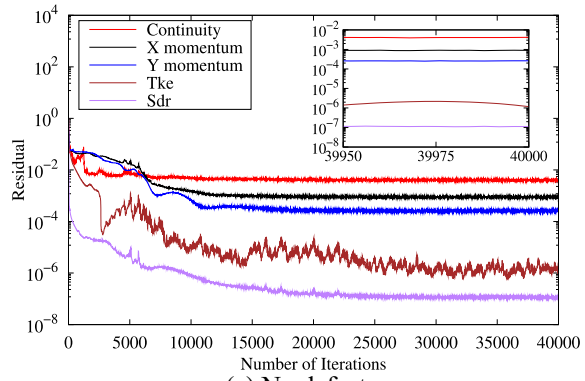

(a) No defect

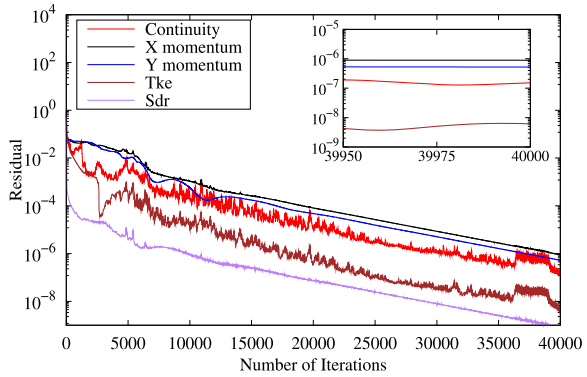

(b) 0.1 mm defect

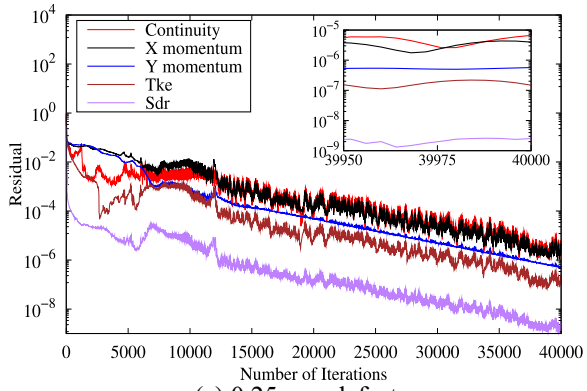

(c) 0.25 mm defect

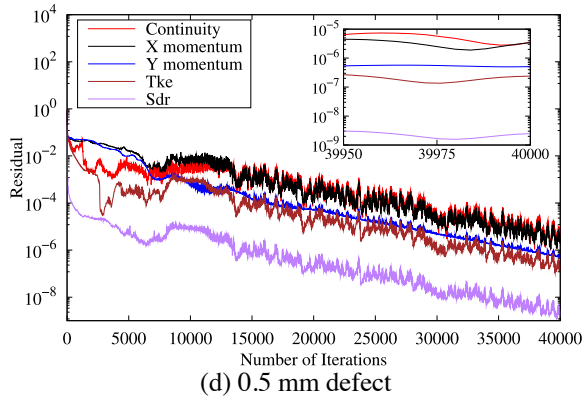

(d) 0.5 mm defect

Figure 13: Residuals for (t/c = 0.0416, f/c = 0.014) without and with defect at $\alpha = 0.8^{\circ}$

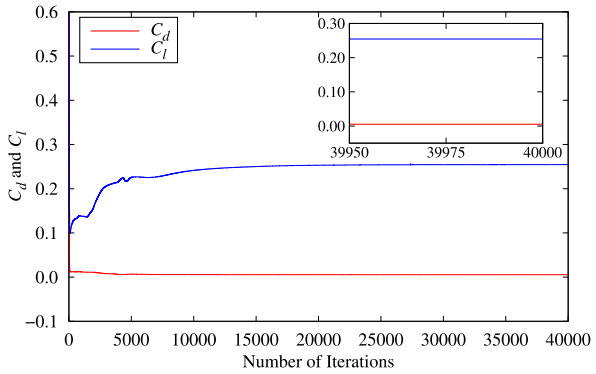

(a) No defect

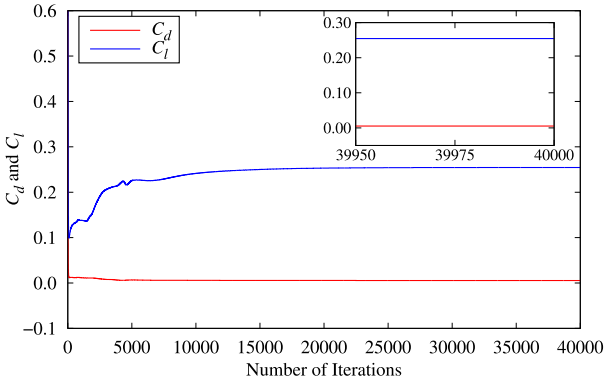

(b) 0.1 mm defect

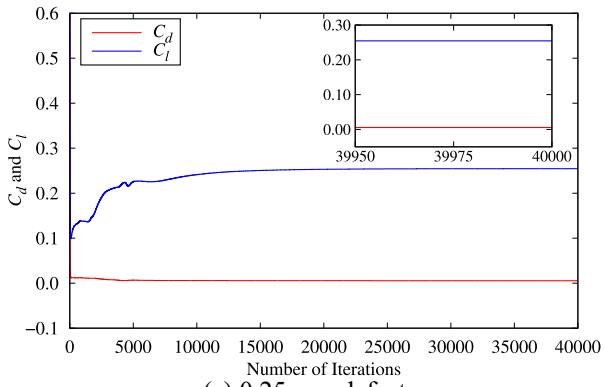

(c) 0.25 mm defect

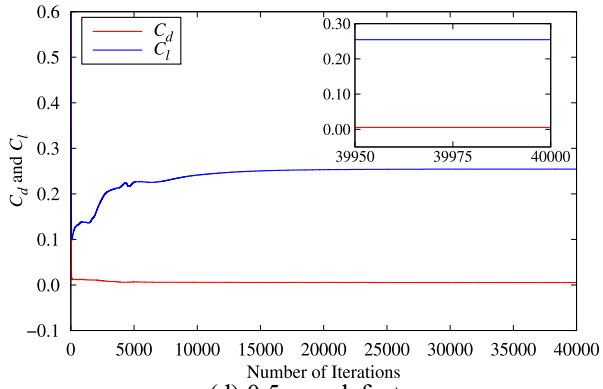

(d) 0.5 mm defect

Figure 14: C_d and C_l for (t/c = 0.0416, f/c = 0.014) without and with defect at $\alpha = 0.8^{\circ}$

Effect of LE Defect on Cavitation Inception Speed

Based on the cavitation buckets for (t/c = 0.0416, f/c = 0.014) as shown in Fig. 10, the reduction percentages in inception speed due to LE defects are presented in Fig. 15 for the foils with defects. In the typical design range of angle of attack ($-1.5^\circ < \alpha < 2.0^\circ$) for a moderately loaded propeller, the reduction in inception speed can reach to 60% for the 0.5 mm defect around $\alpha = 0.75^\circ$. Between 0° and 1.5°, the reduction increases with the size of LE defect. At $1.5^\circ < \alpha < 2.0^\circ$, the reductions for the three defects are around 15% to 20%.

In summary, the LE defects significantly reduce the cavitation inception speeds at the normal range of angle of attack.

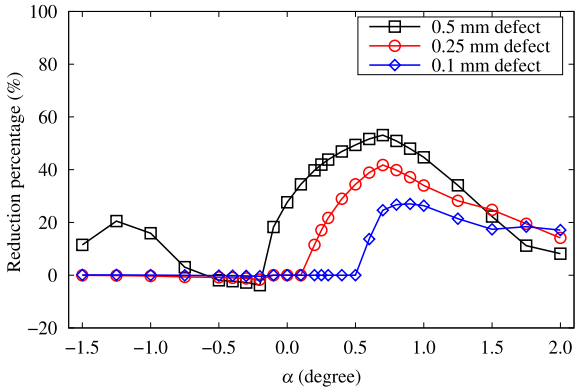

Figure 15: Reduction percentage in cavitation inception speed for the foils with LE defects

Effect of LE Defect on Efficiency

The ratio of lift to drag, i.e. C_l/C_d, of a 2-D section provides an indicator of the hydrodynamic efficiency of the propeller which incorporates it. The effect of a defect on C_l/C_d is shown in Fig. 16. In the normal range of angle of attack for a moderately loaded propeller, the LE defect has little effect on the efficiency. However, at larger angles of attack, for example, a heavily loaded propeller or a propeller operating in a highly uneven wake pattern, a LE defect reduces the efficiency more significantly. A larger LE defect leads to a greater decrease in efficiency.

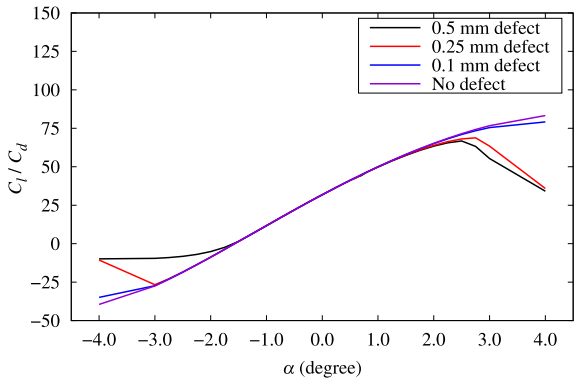

Figure 16: Effect of LE defect on lift-to-drag ratio

CONCLUSIONS

All the LE defects examined are within ISO 484 Class S tolerances (± 0.5 mm for a 1-part template or ± 0.25 mm for the 3-part template). The DTMB modified NACA66 a = 0.8 sections without and with LE defects were investigated at various angles of attack with the 2-D steady RANS solver in Star-CCM+ on structured grids.

Convergence studies were first carried out to examine effects of type of computational domain, domain size, grid distribution, grid resolution, and turbulence model on the solutions. Based on the results of convergence studies, best-practice settings were determined for simulations of 2-D foils using Star-CCM+. With the best-practice settings, studies were carried out to verify the minimum pressure coefficient envelops of (t/c = 0.2, f/c = 0.02) without defect. Numerical results were generally in good agreement with potential-flow solutions by Brockett (1966) and the RANS solutions with ANSYS CFX and TRANSOM by Hally (2018).

CFD simulations using the best-practice settings were extended to (t/c = 0.0416, f/c = 0.014) with three different sizes of defects near the LE, representing three levels of manufacturing tolerances within Class S. The predicted minimum pressure coefficients for the NACA66 sections without and with LE defects were compared at various angles of attack. Comparative studies showed that the LE manufacturing defects of various sizes within ISO Class S have large effects on the cavitation performance of 2-D foil sections in terms of reduced cavitation inception speed in the typical design range of angle of attack. At large angles of attack, these defects will lead to reduction in efficiency.

The following conclusions are made from the 2-D studies:

- Class S defects close to the LE narrow the cavitation buckets in the typical design range of angle of attack, $-1.5^\circ < \alpha < 2^\circ$. As a consequence, such a defective section would experience cavitation which causes URN at a lower speed than the design one. Smaller defects than Class S maximum deviation show a similar effect.
- The detrimental cavitation effect seems to be primarily on the side of the section with the defect. A defect right on the leading edge ($X = 0$ and $Y = 0$) would affect cavitation on both sides of the section.
- The defects can cause pressure drops at the furthest-forward edge of a LE defect. At the upper end of normal range of operations, the section lift decreases and the drag increases resulting in a reduction in propeller efficiency.
- Propeller manufacturing tolerance standards would have to be tighter than ISO Class S so that the cavitation inception speeds of propellers can be within 10% of their design values.

Cavitation tunnel tests of some of these sections with and without defects are planned. The resulting experimental data will be used to confirm these CFD predictions.

ACKNOWLEDGEMENTS

This research was initiated and managed by Dominis Engineering. This work was supported by Transport Canada, MITACS, NSERC, DRDC-Atlantic and Dominis Engineering.

REFERENCES

Salinas, R. *AQUO Project no. 314227, WP 2: Noise sources, impact of propeller noise on global URN, Task T2.5*, 2015.

Van Beek, T. and A. Janssen. "An integrated design and production concept for ship propellers." *In Proceedings of the 34th WEGEMT School "Developments in the Design of Propulsors and Propulsion systems"*, AULA, TUDelft, June, 2000.

Brockett, T. *Minimum pressure envelopes for modified NACA-66 sections with NACA a=0.8 camber and BUSHIPS Type I and Type II sections.* Taylor Naval Ship Research and Development Center, 1966.

CISMaRT. *Report on the CISMaRT/Transport Canada Workshop on ship noise mitigation technologies for a quieter ocean*, 2019.

Gospodnetic, D. and S. Gospodnetic. "Integrated propeller manufacturing system." *12th Symposium on Theory and Practice of Shipbuilding*, Zagreb, Croatia, May 1996.

Gospodnetic, S. "CNC milling of monoblock propellers to final form and finish." *Ottawa Marine Technical Symposium,* Ottawa, Ontario, Feb. 2013.

Gospodnetic, S. "CNC machining of propellers to better than class S tolerances." *SNAME 14th Propeller & Shafting Symposium*, Norfolk, Virginia, Sept. 2015.

Hally, D. "Preliminary CFD simulations of 2-D foils with defects." *DRDC Atlantic Centre,* Canada. 2018.

ISO 484-1. "Shipbuilding – Ship screw propellers – Manufacturing tolerances – Part 1: Propellers of diameter greater than 2.5 m." (2015).

ISO 484-2. "Shipbuilding – Ship screw propellers – Manufacturing tolerances – Part 2: Propellers of diameter between 0.80 and 2.5 m inclusive." (2015).

Janssen, A. and L. Sylvia. "Propeller manufacture and tolerances." *Encyclopedia of Maritime and Offshore Engineering*, (2017): 1-13.

Jones, W. P. and B. E. Launder. "The prediction of laminarization with a two-equation model of turbulence." *International Journal of Heat and Mass Transfer*, 15:2 (1972): 301-314.

Menter, F. "Zonal two equation k-ω turbulence models for aerodynamic flows." *In 23rd Fluid Dynamics, Plasmadynamics, and Lasers Conference*, 1993.

NAVSEA. "Standard propeller drawing, No. 810-4435837, Rev. B." (2004).

Southall, B. L., A. R. Scholik-Schlomer, L. Hatch, T. Bergmann, M. Jasny, K. Metcalf, L. Weilgart and A. J. Wright. "Underwater noise from large commercial ships – international collaboration for noise reduction." *Encyclopedia of Maritime and Offshore Engineering,* (2017): 1-9.

Spalart, P. and S. Allmaras. "A one-equation turbulence model for aerodynamic flows." *In 30th Aerospace Sciences Meeting and Exhibit*. Reno, NV, Jan. 1992.

Tremblay, C. and S. Gospodnetic. "Manufacturing propellers in the 21st century." *Maritime Engineering Journal*, 83 (2017):10-15.

Wilcox, D. C. "Reassessment of the scale-determining equation for advanced turbulence models." *AIAA Journal,* 26:11, (1988): 1299-1310.